Desalination and Water Treatment
www.deswater.com

doi: 10.5004/dwt.2019.23710

145 (2019) 326–336
March

Surface-disorder-engineering-induced enhancement in the photocatalytic activity of $Bi_4Ti_3O_{12}$ nanosheets

Xinxin Zhao[a,b], Hua Yang[a,b,*], Haimin Zhang[b], Ziming Cui[b], Wangjun Feng[b]

[a]*State Key Laboratory of Advanced Processing and Recycling of Non-ferrous Metals, Lanzhou University of Technology, Lanzhou 730050, China, Tel. +86 931 2973783, Fax +86 931 2976040, email: zhaoxinxin7520@163.com (X. Zhao), hyang@lut.cn (H. Yang)*
[b]*School of Science, Lanzhou University of Technology, Lanzhou 730050, China, Tel. +86 931 2973783, Fax +86 931 2976040, email: zh_haimin@tom.com (H. Zhang), 411950619@qq.com (Z. Cui), wjfeng@lut.cn (W. Feng)*

Received 25 July 2018; Accepted 28 December 2018

ABSTRACT

$NaBH_4$ reduction method has been used to create surface disorder on $Bi_4Ti_3O_{12}$ nanosheets with the aim of enhancing their photocatalytic activity. The $NaBH_4$-treated $Bi_4Ti_3O_{12}$ samples were systematically investigated by XRD, TEM, BET, XPS, UV-vis DRS, EIS and transient photocurrent response. It is disclosed that disordered surface layer associated with oxygen vacancy defects is obviously formed on the surface of $Bi_4Ti_3O_{12}$ nanosheets, and simultaneously surface defect states are introduced in the forbidden gap of $Bi_4Ti_3O_{12}$. The $NaBH_4$-treated $Bi_4Ti_3O_{12}$ samples display enhanced visible-light absorption. The photocatalytic performance of the samples was investigated by the degradation of RhB under irradiation of simulated sunlight, UV light and visible light. It is found that the $NaBH_4$-treated $Bi_4Ti_3O_{12}$ samples exhibit a significantly enhanced photocatalytic activity under UV irradiation. The sample treated at 0.1 M $NaBH_4$ solution shows the highest UV photocatalytic activity, about 1.9 times higher than that of pristine $Bi_4Ti_3O_{12}$. This is ascribed to the fact that the induced surface defect states can act as electron acceptors and thus facilitates the separation of photogenerated electron-hole pairs. Moreover, the $NaBH_4$-treated $Bi_4Ti_3O_{12}$ samples also display a slightly enhanced photocatalytic performance under visible light irradiation, which is due to the enhanced visible light absorption induced by the surface defect states.

Keywords: $Bi_4Ti_3O_{12}$ nanosheets; Surface disorder engineering; Surface defect states; Photocatalytic RhB degradation; Photocatalytic mechanism

1. Introduction

During recent years, semiconductor-based photocatalysis has aroused a tremendous interest as a potential green technology to cope with environmental pollution and energy crisis [1–8]. The photocatalysis technology offers many appealing advantages against traditional pollution treatment technologies, such as mild reaction condition, no secondary pollution, simple reaction equipment, low operational cost, good stability and reusability. More importantly, this technology can use sunlight as the power source and requires no consumption of non-renewable energy resources like coal, oil and natural gas. TiO_2 and Ti-contained oxide semiconductors (e.g., $SrTiO_3$, $CaTiO_3$, $BaTiO_3$, $Bi_4Ti_3O_{12}$) are famously known as an important class of photocatalysts, exhibiting powerful capability for photocatalytic decomposition of organic pollutants into harmless inorganic substances and photocatalytic water splitting into hydrogen and/or oxygen [9–13]. However, these Ti-contained oxide semiconductors generally possess a large bandgap (E_g > 3.0 eV) and are photocatalytically active only under ultraviolet (UV) light irradiation. This limits the utilization of solar energy which contains only about 5% UV light. Furthermore, photogenerated electrons (e^-) and holes (h^+) in the semiconductors are easy to be geminately recombined, consequently resulting in low photocatalytic

*Corresponding author.

efficiency. Thus, many strategies have been developed to widen the light-responsive region and facilitate the photogenerated electron-hole pair separation with the aim of enhancing the overall photocatalytic performance of photocatalysts. The most common strategies include doping with impurity elements, decoration with noble metals, construction of heterojunction composites and morphology-mediated tailoring [14–21].

On the other hand, semiconductor-based photocatalysis is intrinsically a heterogeneous surface catalytic reaction, which depends highly on the atomic configuration and electronic structure of exposed crystal facets. Different exposed facets of a semiconductor are expected to manifest different photocatalytic activities since they generally have different surface atomic arrangements, electronic structures and surface energies [22–24]. Moreover, much recent work has shown that the creation of surface-disordered layer and oxygen vacancy defects on the surface of the semiconductor offers a great potential for enhancing its photocatalytic activity [25–31]. Surface defect states are simultaneously introduced in the forbidden energy gap of the semiconductor, which can act as electron acceptors to trap photogenerated electrons and thus effectively hold back the recombination of photogenerated electron-hole pairs [26,27]. Further, the valence band (VB) electrons can be excited to the surface defect states of the semiconductor. This electron transition requires smaller photon energy than that required for the electron transition from the VB to the conduction band (CB) (i.e., interband transition), thus leading to enhanced visible light absorption. As a result, the surface-disorder-engineered semiconductor expectedly manifests enhanced photocatalytic activity under both UV and visible light irradiations. In previous studies, however, there is little research concerned with the surface reconstruction of a special photocatalytically-active facet since most of the synthesized semiconductor nanostructures have a limited exposure of a special active facet.

$Bi_4Ti_3O_{12}$ is one of the most important Ti-contained oxide semiconductors, crystallizing in a special layer structure with perovskite-like $(Bi_2Ti_3O_{10})^{2-}$ blocks alternated by $(Bi_2O_2)^{2+}$ units. Moreover, $Bi_4Ti_3O_{12}$ has an electronic band structure with the VB consisting of O 2p and Bi 6s hybrid orbitals and the CB consisting of Ti 3d and Bi 6p orbitals [32]. Due to its unique layered crystal structure and electronic band structure, $Bi_4Ti_3O_{12}$ exhibits not only promising piezoelectricity, ferroelectricity and photovoltaic property [33–35], but also an important photocatalytic activity toward the degradation of organic pollutants and water splitting into hydrogen [36–51]. To address the photocatalytically active facet, very recently we have synthesized large-sized $Bi_4Ti_3O_{12}$ square nanosheets with nearly 100% exposed (010) facet via a hydrothermal route [52]. The as-synthesized $Bi_4Ti_3O_{12}$ nanosheets were demonstrated to exhibit excellent photocatalytic activity, much superior to that of $Bi_4Ti_3O_{12}$ nanoparticles. In this work, we demonstrate that the photocatalytic activity of $Bi_4Ti_3O_{12}$ nanosheets can be further enhanced by engineering the surface structure of the highly exposed (010) facet with $NaBH_4$ solution treatment. This work offers a promising insight for developing photocatalysts with high photocatalytic activity.

2. Experimental

$Bi_4Ti_3O_{12}$ nanosheets used in the surface treatment were synthesized via a hydrothermal route as described in the literature [52]. Stoichiometric amounts of $TiCl_4$ (0.003 mol), $Bi(NO_3)_3{\cdot}5H_2O$ (0.004 mol) and NaOH (0.12 mol) were dissolved in 20 mL of deionized water, 20 mL of 10% dilute nitric acid solution and 40 mL of deionized water, respectively. The obtained $TiCl_4$ solution and NaOH solution were successively added to the $Bi(NO_3)_3$ solution drop by drop under mild magnetic stirring. The resultant mixture was sealed into a 100 mL Teflon-lined stainless steel autoclave and submitted to heat treatment at 200°C. After 24 h of hydrothermal reaction, the autoclave was naturally cooled to room temperature. The produced precipitate was collected by centrifugation, washed with deionized water (three times) and absolute ethanol (one time), and then dried at 60°C for 12 h to obtain $Bi_4Ti_3O_{12}$ nanosheets. To make the surface treatment of $Bi_4Ti_3O_{12}$, 0.1 g of the as-prepared $Bi_4Ti_3O_{12}$ nanosheets were loaded in 20 mL of $NaBH_4$ solution with concentration varied from 0.05 to 0.2 mol L^{-1} (M), and then magnetically stirred in an ice bath for 40 min. After that, the products were collected by centrifugation, washed with deionized water (three times) and absolute ethanol (one time), and dried at 60°C for 4 h. The samples treated at 0.05, 0.1 and 0.2 M $NaBH_4$ solution were designated as R0.05M-$Bi_4Ti_3O_{12}$, R0.1M-$Bi_4Ti_3O_{12}$ and R0.2M-$Bi_4Ti_3O_{12}$, respectively.

X-ray powder diffraction (XRD) with Cu Kα radiation was used for the phase identification of the samples. Field-emission transmission electron microscopy (TEM) was used to investigate the microstructure of the samples. N_2 adsorption-desorption technique was used to characterize the surface property and Brunauer–Emmett–Teller (BET) surface area of the samples. X-ray photoelectron spectroscopy (XPS) was used to determine the chemical states of elements in the samples. Ultraviolet-visible diffuse reflectance spectroscopy (UV-vis DRS) was used to investigate the optical absorption and bandgap energy of the samples. Electron paramagnetic resonance (EPR) spectra of the samples were measured on a Bruker A300-9.5/12 EPR spectrometer.

The photocurrent response and electrochemical impedance spectroscopy (EIS) of the samples were measured on a CST 350 electrochemical workstation using a three-electrode cell configuration as described in the literature [53]. A platinum foil electrode served as the counter electrode and a standard calomel electrode (SCE) acted as the reference electrode. To prepare the working electrode, 15 mg of the sample ($Bi_4Ti_3O_{12}$ or R0.1M-$Bi_4Ti_3O_{12}$), 0.75 mg of carbon black and 0.75 mg of polyvinylidene fluoride (PVDF) were uniformly mixed together using 1-methyl-2-pyrrolidione (NMP) as solvent. The formed slurry was dispersed homogeneously onto fluorine-doped tin oxide (FTO) glass substrate with an effective area of 1 × 1 cm^2. The electrode was then dried at 60°C for 5 h to obtain the final working electrode. The electrolyte used in this study is a 0.1 M Na_2SO_4 aqueous solution. The transient photocurrent response was measured at a bias potential of 0.2 V. The EIS was measured by applying the sinusoidal voltage pulse with amplitude of 5 mV and in the frequency range from 10^{-2} to 10^5 Hz. A 200 W xenon lamp that emits simulated sunlight was used as the light source.

Rhodamine B (RhB) in aqueous solution was chosen as a model substrate to evaluate the photocatalytic activity of the samples for the pollutant abatement. Simulated sunlight, UV light (λ = 254 nm) and visible light (400 ≤ λ ≤ 780 nm) were separately used as the light source. The initial RhB concentration was 5 mg L^{-1} and the photocatalyst loading was 0.1 g in 100 mL of RhB solution. To examine the adsorption of RhB onto the photocatalyst surface, the mixture was magnetically stirred in the dark for 30 min. After that, the mixture was irradiated to initiate the photocatalytic reaction. To exclude the effect of temperature on the photocatalysis, the reaction solution was maintained at room temperature (21°C) during the photocatalysis process by cooling the reactor with a circulating water cooling system. At intervals of 30 min, 2.5 mL of the reaction solution was withdrawn from the reactor and used for the RhB concentration measurement. The residual concentration of RhB was determined by measuring the absorbance of the reaction solution after removing the photocatalyst at λ = 554 nm on a UV–vis spectrophotometer. The degradation percentage of RhB is given as $(C_0 - C_t)/C_0 \times 100\%$, where C_0 = initial RhB concentration and C_t = residual RhB concentration after reaction for t min.

3. Results and discussion

Fig. 1(a) shows the XRD patterns of $Bi_4Ti_3O_{12}$ before and after treatment with $NaBH_4$ solution of different concentrations. For all the samples, the diffraction peaks can be perfectly indexed according to the $Bi_4Ti_3O_{12}$ orthorhombic phase (PDF#35-0795). This indicates that the dominant crystal structure of $NaBH_4$-treated $Bi_4Ti_3O_{12}$ samples undergoes no change, maintaining the orthorhombic structure identical to that of pristine $Bi_4Ti_3O_{12}$. However, a broad peak at 2θ of 10–20°, which is related to the amorphous nature, is observed for the treated samples. This conforms the formation of disordered surface layer on $Bi_4Ti_3O_{12}$ after $NaBH_4$ treatment. Fig. 1(b)–(e) show the apparent colors of the samples, revealing the color change of $Bi_4Ti_3O_{12}$ from cream white to dark gray after treatment with 0.2 M $NaBH_4$ solution. Moreover, the sample color gradually becomes deeper with increasing the $NaBH_4$ concentration. This color change is ascribed to the creation of disordered surface layer, which is conductive to enhance the visible light absorption.

The microstructures of pristine $Bi_4Ti_3O_{12}$ and R0.1M-$Bi_4Ti_3O_{12}$ were investigated by TEM. Figs. 2a–c show the TEM image, high resolution TEM (HRTEM) image and selected area electron diffraction (SAED) pattern of pristine $Bi_4Ti_3O_{12}$, respectively. It is seen that the untreated $Bi_4Ti_3O_{12}$ nanosheet has a pretty smooth surface and exhibits perfect crystal lattice fringes without internal defects. The lattice fringes with the d-spacing of 0.388 nm correspond to the (202) crystal plane of $Bi_4Ti_3O_{12}$. The SAED pattern in Fig. 2c shows regularly and periodically arranged diffraction spots. Both the SAED pattern and HRTEM image confirm a single-crystalline nature of the $Bi_4Ti_3O_{12}$ nanosheet. Figs. 2d–f show the TEM image, HRTEM image and SAED pattern of R0.1M-$Bi_4Ti_3O_{12}$, respectively. The surface of the $NaBH_4$-treated $Bi_4Ti_3O_{12}$ nanosheet becomes rough and contains numerous irregular pits. This implies that disordered surface layer associated with oxygen vacancy defects is created on $Bi_4Ti_3O_{12}$. However, the basic orthorhombic lattice structure of $Bi_4Ti_3O_{12}$ is not destroyed since the lattice fringes of the $Bi_4Ti_3O_{12}$ (202) crystal plane are still clearly visible from the HRTEM image. Moreover, the SAED pattern in Fig. 2f shows that the dominant diffraction spots are periodically arranged in an array identical to that of pristine $Bi_4Ti_3O_{12}$ as shown in Fig. 2c, further indicating no destruction to the basic lattice structure of $Bi_4Ti_3O_{12}$. The additional weak diffraction spots observed in the SAED pattern are attributed to minor small $Bi_4Ti_3O_{12}$ particles attached on the surface of the nanosheet.

Fig. 3 shows the N_2 adsorption-desorption isotherms of pristine $Bi_4Ti_3O_{12}$ and R0.1M-$Bi_4Ti_3O_{12}$. The inset shows the corresponding pore size distribution curves derived from the adsorption branch of the isotherms using the Barrett–Joyner–Halenda (BJH) method. Both the isotherms belong to type II according to the IUPAC classification [54]. The isotherm of pristine $Bi_4Ti_3O_{12}$ shows almost no hysteresis

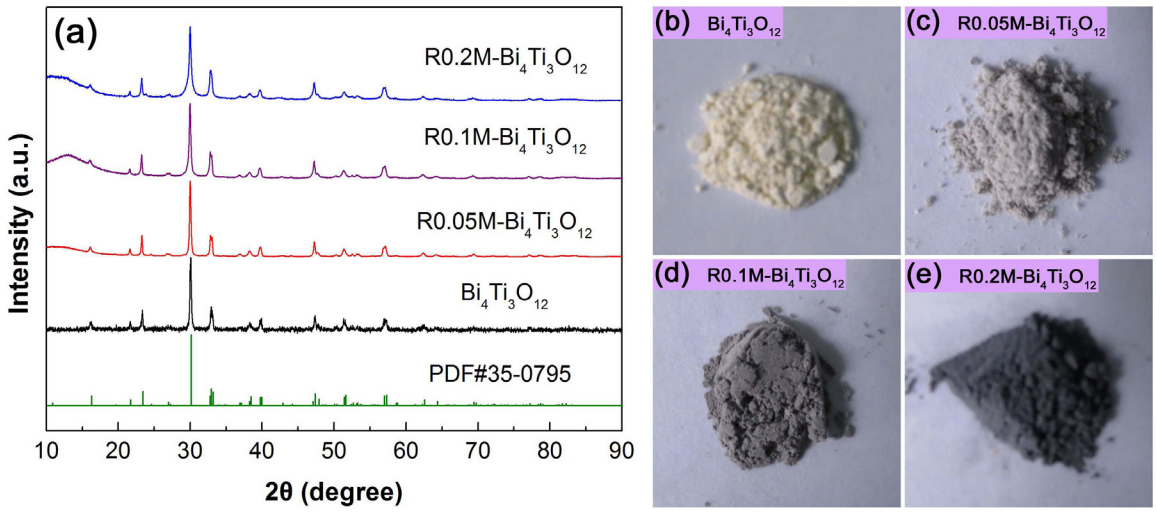

Fig. 1. XRD patterns (a) and digital images (b)–(e) of $Bi_4Ti_3O_{12}$ before and after treatment with $NaBH_4$ solution of different concentrations.

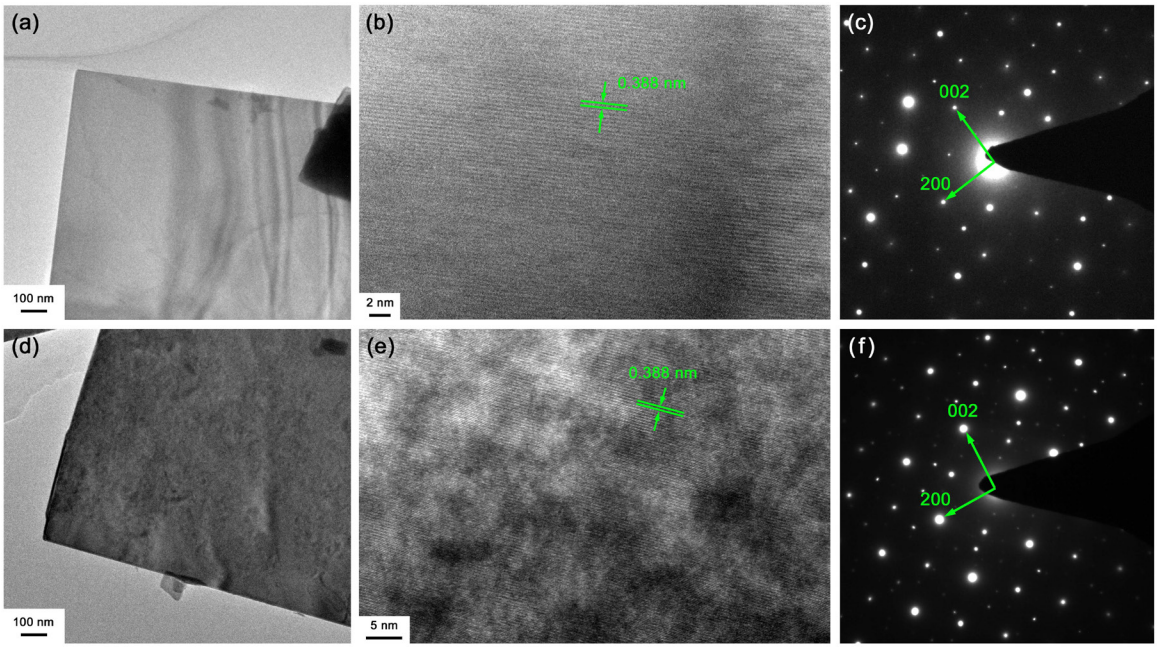

Fig. 2. (a), (b) and (c) TEM image, HRTEM image and SAED pattern of pristine $Bi_4Ti_3O_{12}$, respectively. (d), (e) and (f) TEM image, HRTEM image and SAED pattern of R0.1M-$Bi_4Ti_3O_{12}$, respectively.

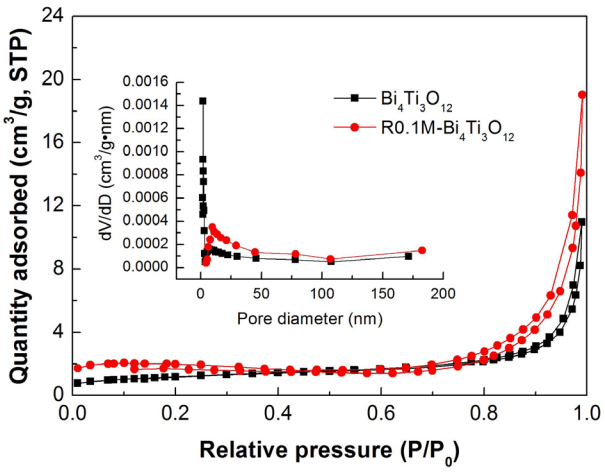

Fig. 3. N_2 adsorption-desorption isotherms of pristine $Bi_4Ti_3O_{12}$ and R0.1M-$Bi_4Ti_3O_{12}$. The inset shows the corresponding pore size distribution curves derived from the adsorption branch of the isotherms using the BJH method.

loop with good coincidence between desorption curve and adsorption curve, whereas the isotherm of R0.1M-$Bi_4Ti_3O_{12}$ displays a small hysteresis loop of type H3 at a high relative pressure range of 0.6–1.0. This implies the possible existence of mesopores in R0.1M-$Bi_4Ti_3O_{12}$. The pore size distribution curves reveal that pristine $Bi_4Ti_3O_{12}$ has slit like pores of ca. 2 nm while R0.1M-$Bi_4Ti_3O_{12}$ contains mesopores with size of 5–45 nm. The appearance of mesopores in R0.1M-$Bi_4Ti_3O_{12}$ is attributed to the etching pits on its surface created by $NaBH_4$ solution treatment. The BET surface area of $Bi_4Ti_3O_{12}$ and R0.1M-$Bi_4Ti_3O_{12}$ is obtained as 4.22 and 6.54 $m^2 g^{-1}$, respectively.

Fig. 4a shows the UV-vis DRS spectra of $Bi_4Ti_3O_{12}$ before and after treatment with $NaBH_4$ solution of different concentrations. Compared to pristine $Bi_4Ti_3O_{12}$, $NaBH_4$-treated $Bi_4Ti_3O_{12}$ samples exhibit significantly enhanced visible light absorption, and moreover, the visible light absorption of the samples exhibits an increasing trend with increasing the $NaBH_4$ concentration. This is consistent with the apparent color change of the samples gradually from cream white to dark gray. The enhanced visible light absorption of $NaBH_4$-treated $Bi_4Ti_3O_{12}$ samples favors the utilization of visible light during the photocatalysis. The absorption edge of the samples, corresponding to the electron transition from the VB to the CB, can be derived from the first derivative UV-vis DRS spectra of the samples, as shown in Fig. 4(b). According to the peak on the spectra, the bandgap energy (E_g) of pristine $Bi_4Ti_3O_{12}$, R0.05M-$Bi_4Ti_3O_{12}$, R0.1M-$Bi_4Ti_3O_{12}$ and R0.2M-$Bi_4Ti_3O_{12}$ is obtained as 3.13, 3.29, 3.39 and 3.48 eV, respectively. It is seen that $NaBH_4$-treated $Bi_4Ti_3O_{12}$ samples have a bandgap energy larger than that of pristine $Bi_4Ti_3O_{12}$. This could be ascribed to the fact that the creation of disordered surface layer and oxygen vacancy defects could result in the lattice expansion and hence cause an increase in the bandgap energy.

The chemical states of elements in $Bi_4Ti_3O_{12}$ and R0.1M-$Bi_4Ti_3O_{12}$ were investigated by XPS. The binding energy scale of the XPS data was calibrated according to the C 1s peak at 284.8 eV. As seen from Fig. 5a, R0.1M-$Bi_4Ti_3O_{12}$ shows a Bi 4f XPS spectrum very similar to that of pristine $Bi_4Ti_3O_{12}$. The peaks at 159.0 and 164.3 eV are assigned to the binding energies of Bi $4f_{7/2}$ and Bi $4f_{5/2}$, respectively [46,47], implying the existence of Bi^{3+} oxidation state. Dong et al. reported Bi nanowires@BiOCl nanosheets by reduction of partial Bi^{3+} on the surface of BiOCl using the NaBH4 reduction method [55]. However, Bi metal reduced from Bi^{3+} on the $NaBH_4$-treated $Bi_4Ti_3O_{12}$ can be negligible since no addi-

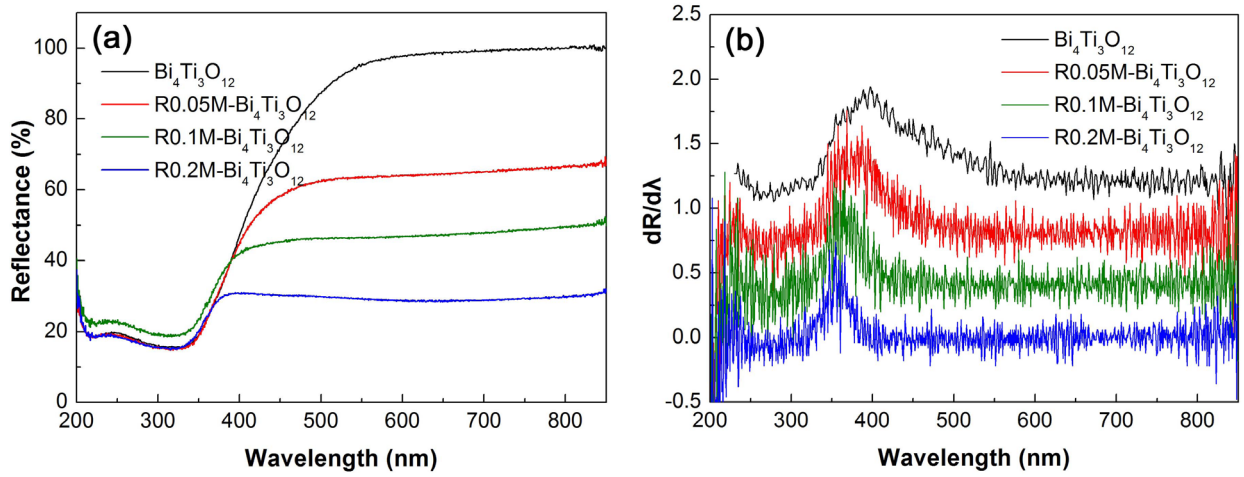

Fig. 4. UV-vis DRS spectra (a) and the corresponding first derivatives (b) of $Bi_4Ti_3O_{12}$ before and after treatment with $NaBH_4$ solution of different concentrations.

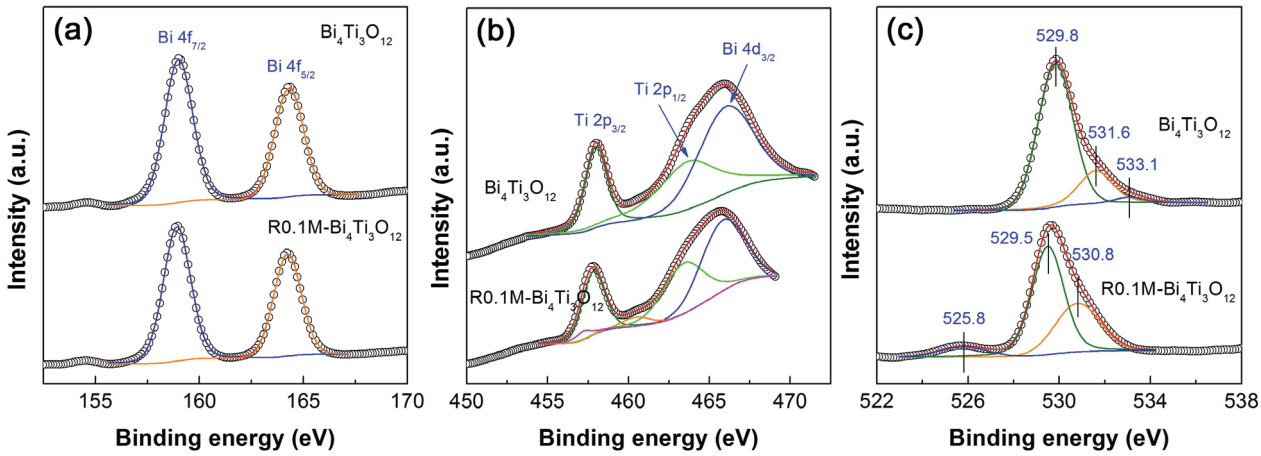

Fig. 5. XPS spectra of pristine $Bi_4Ti_3O_{12}$ and R0.1M-$Bi_4Ti_3O_{12}$. (a) Bi 4f XPS spectra; (b) Ti 2p XPS spectra; (c) O 1s XPS spectra.

tional peaks are detected in the Bi 4f XPS spectra. Fig. 5b shows the Ti 2p XPS spectra of $Bi_4Ti_3O_{12}$ and R0.1M-$Bi_4Ti_3O_{12}$. It is noted that the binding energy of Ti $2p_{1/2}$ is very close to the binding energy of Bi $4d_{3/2}$, thus leading to a partial overlapping of Ti $2p_{1/2}$ and Bi $4d_{3/2}$ peaks [40,46,47]. As a result, a broad bump at around 465 eV is observed on the Ti 2p spectra. The binding energy of Ti $2p_{1/2}$ can be derived by the peak deconvolution. The binding energies of Ti $2p_{3/2}$ and Ti $2p_{1/2}$ for pristine $Bi_4Ti_3O_{12}$ are observed at 458.0 and 463.6 eV, respectively, implying that titanium element is in the form of Ti^{4+} oxidation state . For R0.1M-$Bi_4Ti_3O_{12}$, the binding energies of Ti $2p_{3/2}$ and Ti $2p_{1/2}$ are observed at 457.8 and 463.4 eV, respectively, which are slightly smaller than those for pristine $Bi_4Ti_3O_{12}$. This could be attributed to the increase in the Ti–O bond length of $NaBH_4$-treated $Bi_4Ti_3O_{12}$, which is in accord with the observed increase of the bandgap energy. Moreover, two additional small peaks appears at 457.2 and 460.5 eV, which are characterized as $2p_{3/2}$ and $2p_{1/2}$ of Ti^{3+}, respectively [25]. The presence of Ti^{3+} oxidation state implies the formation of oxygen vacancies at the surface of $Bi_4Ti_3O_{12}$ nanosheets. From Fig. 5c it is seen that the O 1s XPS spectrum of $Bi_4Ti_3O_{12}$ is deconvoluted into three peaks at 529.8, 531.6 and 533.1 eV. The binding energy at 529.8 eV is attributed to the crystal lattice oxygen of $Bi_4Ti_3O_{12}$. The peaks at higher binding energies of 531.6 and 533.1 eV could arise from chemisorbed oxygen species and water species, respectively [47]. For R0.1M-$Bi_4Ti_3O_{12}$, the O 1s binding energy of the lattice oxygen is observed at 529.5 eV, which is slightly smaller than that for pristine $Bi_4Ti_3O_{12}$. This could be interpreted as a result of the increased Ti–O bond length induced by $NaBH_4$ treatment, as also evidenced by Ti 2p XPS spectra and UV-vis DRS spectra. The binding energy peak at 530.8 eV corresponding to chemisorbed oxygen species becomes obviously more intensive than that of pristine $Bi_4Ti_3O_{12}$. Generally, the chemisorbed oxygen species is induced by oxygen vacancy defects [26,31]. The observed increase in the intensity of the O 1s peak related to the chemisorbed oxygen species indicates the creation of oxygen vacancies at the surface of $NaBH_4$-treated $Bi_4Ti_3O_{12}$ nanosheets. The observed prepeak at 525.8 eV is possibly induced due to the existence of holes on O 2p orbitals [56].

EPR spectroscopy is an important technology that can be used to determine oxygen vacancies formed in semiconductor photocatalysts. The formation of oxygen vacancies is generally associated with the signal at Lande factor g = 2 [57]. Fig. 6 shows the EPR spectra of $Bi_4Ti_3O_{12}$ and R0.1M-$Bi_4Ti_3O_{12}$ (magnetic-field frequency ν = 9.429737 GHz). No obvious signal is observed for $Bi_4Ti_3O_{12}$, whereas a weak signal peak at g = 2 is observed for R0.1M-$Bi_4Ti_3O_{12}$, implying the production of minor oxygen vacancies in $NaBH_4$-treated $Bi_4Ti_3O_{12}$. The appearance of signal peak at lower magnetic field (or higher Lande factor) could be attributed to the formation of minor Ti^{3+} oxidation state in R0.1M-$Bi_4Ti_3O_{12}$, as revealed by Ti 2p XPS spectrum.

The photocurrent responses and EIS spectra of the samples were investigated to elucidate the separation and transfer behavior of photogenerated electrons and holes. Fig. 7a shows the transient photocurrent response curves of pristine $Bi_4Ti_3O_{12}$ and R0.1M-$Bi_4Ti_3O_{12}$ recorded for several on/off cycles of intermittent simulated sunlight irradiation. On irradiation with the simulated sunlight, pristine $Bi_4Ti_3O_{12}$ demonstrates a photocurrent density of ca. 0.05 μA cm^{-2} while R0.1M-$Bi_4Ti_3O_{12}$ has a photocurrent density of ca. 0.35–0.40 μA cm^{-2}. After turning off the light, the photocurrent density for both samples drops to a very low level. This transient photocurrent response appears to be very reproducible when alternately turning on and turning off the light. The higher photocurrent density observed for R0.1M-$Bi_4Ti_3O_{12}$ suggests that $NaBH_4$-treated $Bi_4Ti_3O_{12}$ exhibits an enhanced electron-hole pair separation when compared with pristine $Bi_4Ti_3O_{12}$. Fig. 7b shows the Nyquist plots of the EIS spectra for pristine $Bi_4Ti_3O_{12}$ and R0.1M-$Bi_4Ti_3O_{12}$, both of which are shaped like a semicircle. The diameter of the semicircle is associated with the charge-transfer resistance at the electrode/electrolyte interface, and a smaller diameter means a smaller charge-transfer resistance [58]. Compared to pristine $Bi_4Ti_3O_{12}$, R0.1M-$Bi_4Ti_3O_{12}$ obviously displays a smaller charge-transfer resistance as evidenced from the EIS spectra, implying that $NaBH_4$-treated $Bi_4Ti_3O_{12}$ exhibits more efficient electron-hole separation and faster interface charge transfer under simulated sunlight irradiation.

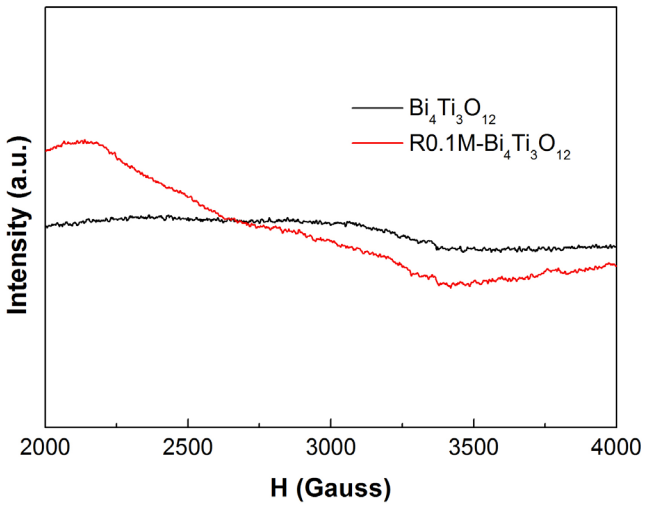

Fig. 6. EPR spectra of $Bi_4Ti_3O_{12}$ and R0.1M-$Bi_4Ti_3O_{12}$.

Simulated sunlight, UV light (λ = 254 nm) and visible light (400 ≤ λ ≤ 780 nm) were separately used as the light source to evaluate the degradation of RhB catalyzed by $Bi_4Ti_3O_{12}$ samples. Prior to the photocatalysis, the dye adsorption was measured in the dark at 30 min of contact time and is obtained to be 8% for pristine $Bi_4Ti_3O_{12}$ and 9–12% for $NaBH_4$-treated $Bi_4Ti_3O_{12}$ samples. The slightly increased dye adsorption onto $NaBH_4$-treated samples could be ascribed to their increased surface area, as evidenced by the BET analysis. Fig. 8a shows the time-dependent photocatalytic degradation of RhB under simulated sunlight irradiation. It is seen that $NaBH_4$-treated $Bi_4Ti_3O_{12}$ samples exhibit obviously higher photocatalytic performance than pristine $Bi_4Ti_3O_{12}$. With increasing the $NaBH_4$ concentration from 0.05 to 0.2 M, the highest photocatalytic performance is observed for R0.1M-$Bi_4Ti_3O_{12}$ that is treated at 0.1 M $NaBH_4$ solution. After 120 min of photocatalysis, 92.3% of the dye is seen to be degraded over R0.1M-$Bi_4Ti_3O_{12}$, whereas only 74.6% of the dye is degraded over pris-

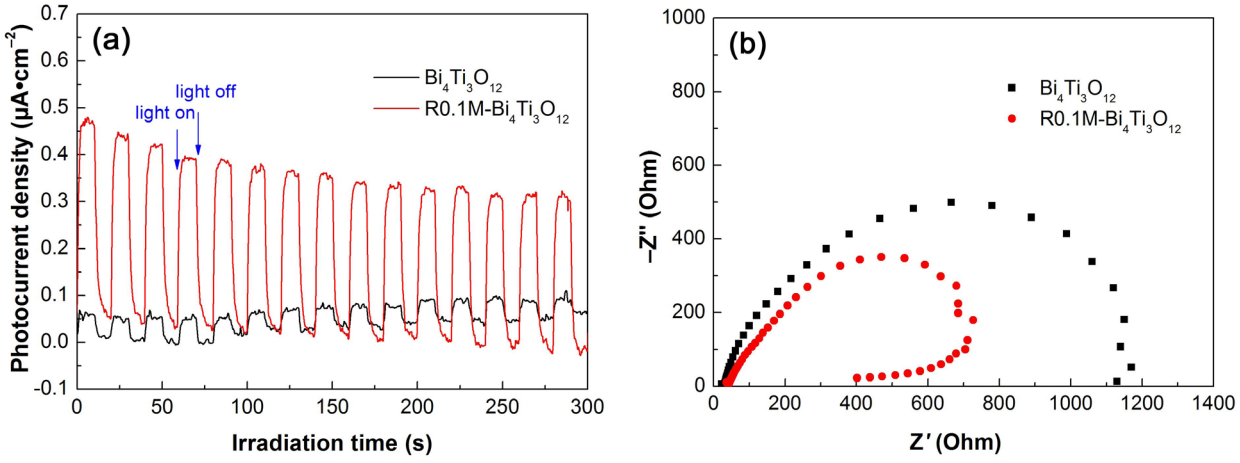

Fig. 7. (a) Transient photocurrent responses of pristine $Bi_4Ti_3O_{12}$ and R0.1M-$Bi_4Ti_3O_{12}$ under intermittent irradiation of simulated sunlight. (b) Nyquist plots of the EIS spectra of pristine $Bi_4Ti_3O_{12}$ and R0.1M-$Bi_4Ti_3O_{12}$ under simulated sunlight irradiation.

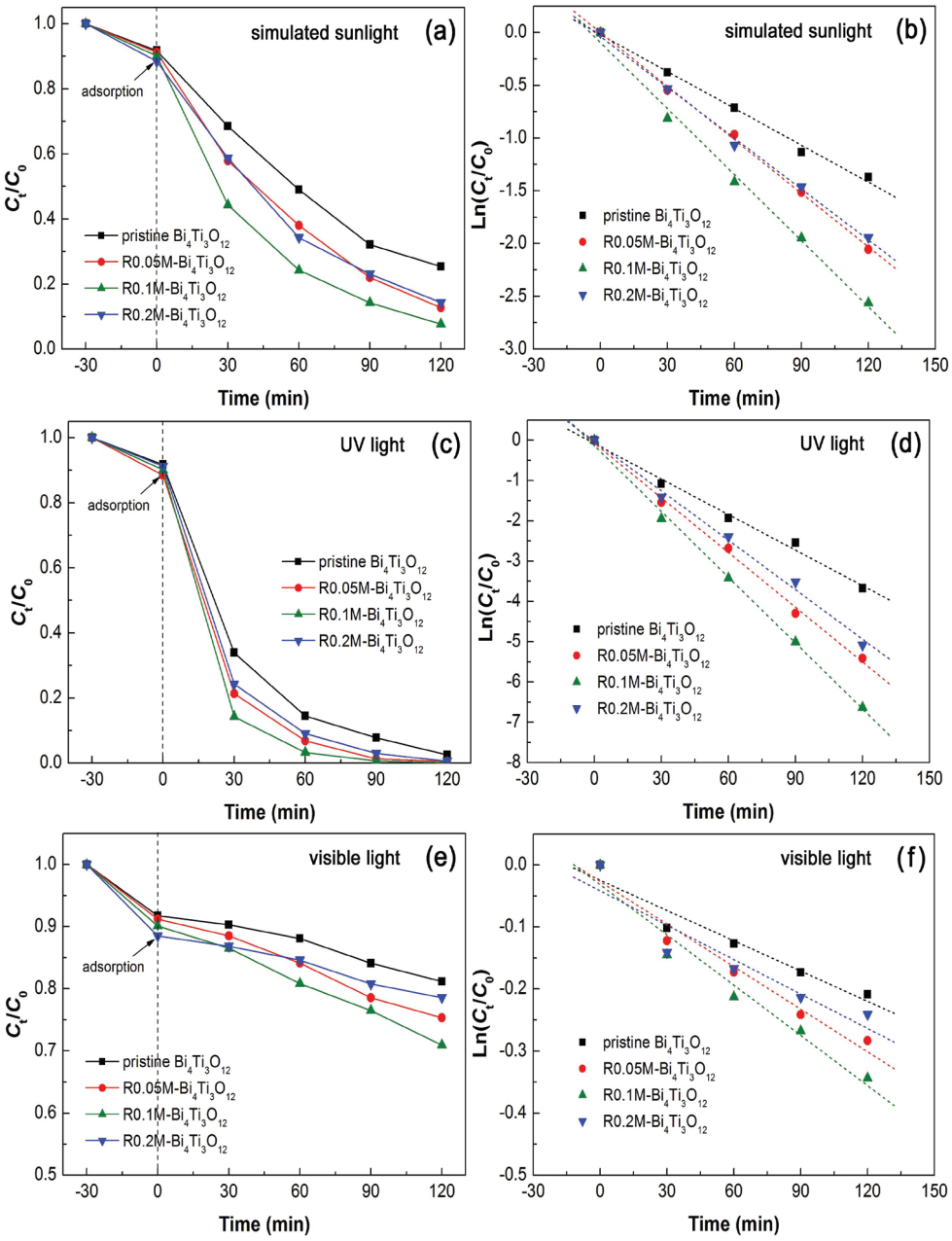

Fig. 8. (a), (c) and (e) Time-dependent photocatalytic degradation of RhB over $Bi_4Ti_3O_{12}$ samples under irradiation of simulated sunlight, UV light (λ = 254 nm) and visible light (400 ≤ λ ≤ 780 nm), respectively. (b), (d) and (f) Plots of $Ln(C_t/C_0)$ *vs* irradiation time *t* for the simulated sunlight, UV light and visible light degradation of RhB, respectively.

tine $Bi_4Ti_3O_{12}$ (Table 1). To further reveal the photocatalytic activity of the samples, Fig. 8b shows the kinetics plots of the dye degradation under simulated sunlight irradiation. The $Ln(C_t/C_0)$ plots exhibit a nearly linear variation against *t* and can be described by pseudo first-order kinetics equation: $Ln(C_t/C_0) = -k_{app}t$, where k_{app} is the apparent first-order reaction rate constant (min^{-1}) [59]. From the slope of the regression lines, the rate constant is obtained, as shown in Table 1. It is demonstrated that R0.1M-$Bi_4Ti_3O_{12}$ has a photocatalytic activity ca. 1.8 times higher than pristine $Bi_4Ti_3O_{12}$ under simulated sunlight irradiation. Figs. 8c and d show the photocatalytic performance of $Bi_4Ti_3O_{12}$ samples under UV irradiation, revealing that pristine $Bi_4Ti_3O_{12}$ is an excellent UV active photocatalyst, and further, the UV photocatalytic activity of $Bi_4Ti_3O_{12}$ is significantly enhanced after surface-treated by $NaBH_4$. After UV photocatalytic reaction for 120 min, the dye degradation reaches 97.5% for pristine $Bi_4Ti_3O_{12}$ and 99.9% for R0.1M-$Bi_4Ti_3O_{12}$. The reaction rate constant suggests that the latter has a UV photocatalytic activity ca. 1.9 times higher than the former. Figs. 8e and f show the photocatalytic degradation of RhB over $Bi_4Ti_3O_{12}$ samples under visible light irradiation. It is seen

Table 1
Degradation percentage of RhB (reaction for 120 min) and apparent first-order reaction rate constant catalyzed by $Bi_4Ti_3O_{12}$ samples under irradiation of simulated sunlight, UV and visible light

Samples	Bandgap (eV)	Simulated sunlight		UV light		Visible light	
		Degradation (%)	k_{app} (min^{-1})	Degradation (%)	k_{app} (min^{-1})	Degradation (%)	k_{app} (min^{-1})
Pristine $Bi_4Ti_3O_{12}$	3.13	74.6	0.01166	97.5	0.02941	18.8	0.00163
R0.05M-$Bi_4Ti_3O_{12}$	3.29	87.2	0.01692	99.6	0.04092	24.7	0.00229
R0.1M-$Bi_4Ti_3O_{12}$	3.39	92.3	0.02085	99.9	0.05442	29.1	0.0027
R0.2M-$Bi_4Ti_3O_{12}$	3.48	85.7	0.01606	99.4	0.04527	21.4	0.00185

that pristine $Bi_4Ti_3O_{12}$ exhibits little visible-light photocatalytic activity and only 18.8% of the dye is degraded. The slight degradation of the dye could be attributed to the dye photosensitization under visible light irradiation. In contrast, $NaBH_4$-treated $Bi_4Ti_3O_{12}$ samples demonstrate slightly increased visible-light photocatalytic activity and the dye degradation reaches 29.1% for the optimal R0.1M-$Bi_4Ti_3O_{12}$ sample. The slight increase in the visible-light photocatalytic activity of $NaBH_4$-treated $Bi_4Ti_3O_{12}$ samples is attributed to their enhanced visible light absorption, as evidenced from the UV-vis DRS spectra.

The reusability of $NaBH_4$-treated $Bi_4Ti_3O_{12}$ was investigated by the recycling photocatalytic degradation of RhB under simulated sunlight irradiation. When the first cycle of the photocatalytic experiment was completed, the photocatalyst was collected by centrifugation, washed with deionized water and then dried at 60°C for 5 h. The recovered photocatalyst was used for the next cycle of the photocatalytic experiment under the same conditions. Fig. 9 shows four cycles of the photocatalytic degradation of RhB catalyzed by R0.1M-$Bi_4Ti_3O_{12}$. At the 4th cycle of the photocatalysis, the dye degradation still maintains a high level of 87.8% at 120 min of reaction, implying a good photocatalytic stability of R0.1M-$Bi_4Ti_3O_{12}$.

To reveal the reactive species including hydroxyl (•OH), superoxide ($•O_2^-$) and h^+, reactive species trapping experiments were carried out, where ethanol, benzoquinone (BQ) and ammonium oxalate (AO) were used as the scavengers of •OH, $•O_2^-$ and h^+, respectively [60]. Fig. 10 shows the effect of ethanol (5 mL), BQ (1 mM) and AO (1 mM) on the degradation of RhB over R0.1M-$Bi_4Ti_3O_{12}$ under simulated sunlight irradiation. It is demonstrated that the dye degradation is significantly suppressed on the addition of AO to the reaction solution, implying that the dye degradation is highly dependent on h^+. In contrast, the addition of ethanol or BQ has a minor effect on the dye degradation, suggesting that •OH and $•O_2^-$ play only a minor role in the photocatalysis. Moreover, we also examined •OH, which is a strong oxidizer existing in most photocatalytic systems, by photoluminescence spectroscopy using terephthalic acid as a probe molecule of •OH [61], and no •OH was found to be produced in the R0.1M-$Bi_4Ti_3O_{12}$ photocatalytic system.

$Bi_4Ti_3O_{12}$ is known to be an intrinsic n-type semiconductor. The conduction band (CB) potential of $NaBH_4$-treated $Bi_4Ti_3O_{12}$ (e.g. R0.1M-$Bi_4Ti_3O_{12}$), which is roughly equal to its flat band potential V_{FB}, can be derived from the Mott–Schottky plots, as shown in Fig. 11a. The Mott–Schottky plots were obtained by the EIS measurement at different

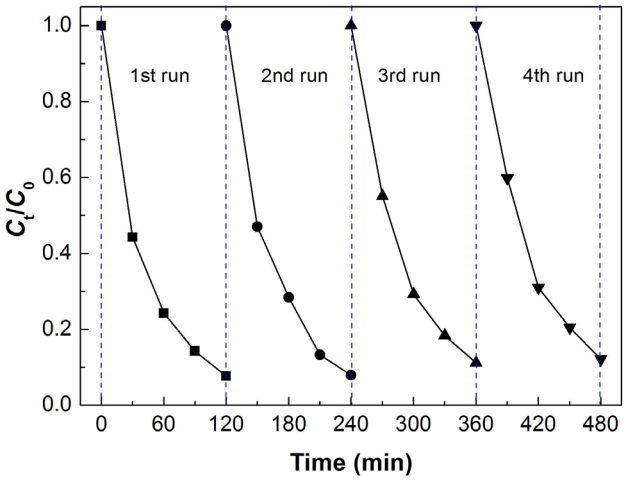

Fig. 9. Photocatalytic degradation of RhB over R0.1M-$Bi_4Ti_3O_{12}$ repeatedly used for four times.

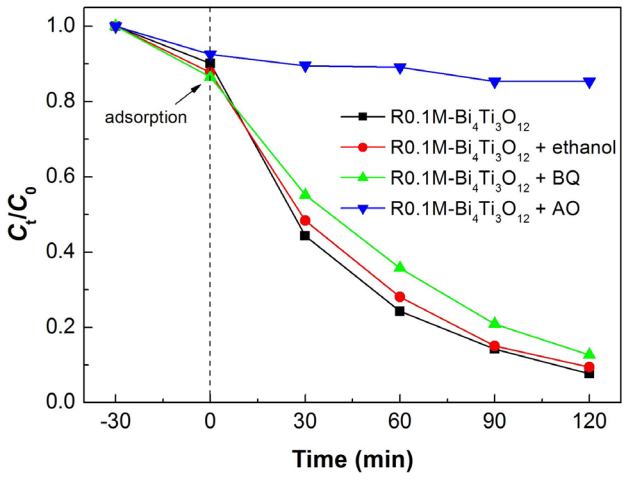

Fig. 10. Effect of ethanol, BQ and AO on the degradation of RhB over R0.1M-$Bi_4Ti_3O_{12}$ under simulated sunlight irradiation.

applied potentials (V) in the dark according to the method as described in the literature [62–64]. By extrapolating the linear portion of the plots to the V axis, the V_{FB} can be determined. As shown in Fig. 11a, the Mott–Schottky plots measured at different frequencies (5000 and 8000 Hz) yield a

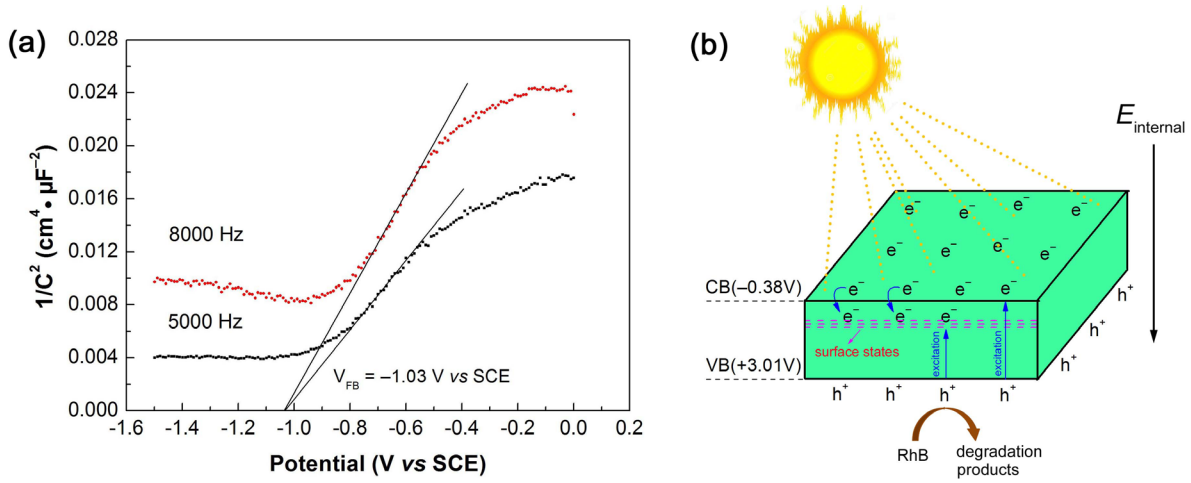

Fig. 11. (a) Mott–Schottky plots of R0.1M-$Bi_4Ti_3O_{12}$ obtained at different frequencies. (b) Schematic illustration of the photocatalytic mechanism for surface-engineered $Bi_4Ti_3O_{12}$ nanosheets.

similar V_{FB} value of –1.03 V *vs* SCE. The potential *vs* SCE reference electrode can be converted to the potential *vs* normal hydrogen electrode (NHE) according to *V*(NHE) = *V*(SCE) + 0.059pH + 0.242 (here pH = 7) [64]. Further considering that the bandgap of R0.1M-$Bi_4Ti_3O_{12}$ is 3.39 eV, the CB and valence band (VB) potentials of R0.1M-$Bi_4Ti_3O_{12}$ are therefore obtained as –0.38 V and +3.01 V *vs* NHE, respectively. It is seen that the CB potential of $Bi_4Ti_3O_{12}$ is very close to the redox potential of $O_2/{}^{\bullet}O_2^-$ (–0.33 V *vs* NHE) [38]. Moreover, the photogenerated electrons will be trapped by the surface defect states, which have potentials more positive than the redox potential of $O_2/{}^{\bullet}O_2^-$, as shown in Fig. 11b. This suggests that ${}^{\bullet}O_2^-$ is difficult to be produced in the R0.1M-$Bi_4Ti_3O_{12}$ photocatalytic system from the thermodynamic viewpoint. As a result, ${}^{\bullet}O_2^-$ plays only a minor role in the photocatalysis, as shown by the reactive species trapping experiment. The VB potential of $Bi_4Ti_3O_{12}$ is positive to the redox potentials of $H_2O/{}^{\bullet}OH$ (+2.38 V *vs* NHE) and $OH^-/{}^{\bullet}OH$ (+1.99 V *vs* NHE) [53], implying that the photogenerated holes can thermodynamically react with OH^-/H_2O to produce ${}^{\bullet}OH$. However, no ${}^{\bullet}OH$ was detected in the present photocatalytic system and moreover the reactive species trapping experiment shows a minor or negligible role of ${}^{\bullet}OH$ in the photocatalysis. This implies that direct hole oxidation is the dominant mechanism causing the dye degradation.

Based on the above experimental results and analysis, a possible mechanism for the enhanced photocatalytic activity of $NaBH_4$-treated $Bi_4Ti_3O_{12}$ is proposed, as schematically illustrated in Fig. 11b. When $Bi_4Ti_3O_{12}$ is treated by $NaBH_4$ solution of appropriate concentrations, disordered surface layer associated with oxygen vacancy defects is created the surface of $Bi_4Ti_3O_{12}$ nanosheets, and simultaneously surface defect states are introduced in the forbidden gap of $Bi_4Ti_3O_{12}$. When illuminated by UV light, the VB electrons are excited to the CB (mainly for bulk electrons) or surface defect states (mainly for surface electrons) of $Bi_4Ti_3O_{12}$. The photogenerated electrons in the CB are expected to be trapped by the surface defect states since the surface defect states can act as electron acceptors [26,27]. As a result, the recombination of photogenerated electrons and holes is effectively suppressed, which is clearly evidenced by the photocurrent response and EIS analyses. More photogenerated holes are therefore available to participate in the photocatalytic reactions. This is the dominant reason that $NaBH_4$-treated $Bi_4Ti_3O_{12}$ samples exhibit significantly enhanced UV photocatalytic activity when compared with pristine $Bi_4Ti_3O_{12}$. On the other hand, under irradiation of visible light ($400 \le \lambda \le 780$ nm), the VB electrons cannot be excited to the CB of $Bi_4Ti_3O_{12}$ due to its large bandgap (3.13 eV for pristine $Bi_4Ti_3O_{12}$). Consequently little visible-light photocatalytic activity is observed for pristine $Bi_4Ti_3O_{12}$. Whereas for $NaBH_4$-treated $Bi_4Ti_3O_{12}$ samples, the visible light irradiation can induce the electron excitation from the VB to the surface defect states (mainly for surface electrons), thus extending the light absorption region as revealed by UV-vis DRS spectra. As a result, $NaBH_4$-treated $Bi_4Ti_3O_{12}$ samples exhibit slightly enhanced visible-light photocatalytic activity. Further, the BET analysis suggests that $NaBH_4$-treated $Bi_4Ti_3O_{12}$ samples have a BET surface area larger than that of pristine $Bi_4Ti_3O_{12}$, which is also beneficial to improve the photocatalytic performance. With increasing the $NaBH_4$ concentration, the optimal sample with the highest photocatalytic performance is observed for R0.1M-$Bi_4Ti_3O_{12}$ that is treated at 0.1 M $NaBH_4$ solution. However, further increasing the $NaBH_4$ concentration leads to decease in the photocatalytic performance of the treated $Bi_4Ti_3O_{12}$ samples. This is possibly due to the fact that bulk defects could be created in $Bi_4Ti_3O_{12}$, which could act as charge carrier recombination centers and facilitate the recombination of photogenerated electron-hole pairs [28,31]. Finally, it is pointed out that the polarization electric field (or internal electric field) of the $Bi_4Ti_3O_{12}$ nanosheet is perpendicular to its plane [65], as shown in Fig. 11b. Under the action of the polarization electric field, photogenerated electrons and holes are readily separated and migrate to the opposite planes of the nanosheet. This suggests that surface-engineered $Bi_4Ti_3O_{12}$ nanosheets offer much more advantage in achieving excellent photocatalytic performance than other surface-engineered semiconductor photocatalysts.

4. Conclusions

Disordered surface layer associated with oxygen vacancy defects was created on the surface of $Bi_4Ti_3O_{12}$ nanosheets via a $NaBH_4$ reduction method. Simultaneously, surface defect states are introduced in the forbidden gap of $Bi_4Ti_3O_{12}$, which can act as electron acceptors and facilitates the separation of photogenerated electrons and holes. As a result, the surface disorder-engineered $Bi_4Ti_3O_{12}$ samples exhibit a significantly enhanced photocatalytic activity toward the degradation of RhB under UV irradiation. The highest UV photocatalytic activity is observed for the sample treated at 0.1 M $NaBH_4$ solution, which is about 1.9 times higher than that of pristine $Bi_4Ti_3O_{12}$. Moreover, the surface disorder-engineered $Bi_4Ti_3O_{12}$ samples also display a slightly enhanced photocatalytic activity under visible light irradiation. This can be explained as the result of enhanced visible light absorption due to the electron excitation from the VB to the surface defect states.

Acknowledgements

This work was supported by the National Natural Science Foundation of China (Grant No. 51662027).

References

[1] M.R. Hoffmann, S.T. Martin, W. Choi, D.W. Bahemann, Environmental applications of semiconductor photocatalysis, Chem. Rev., 95 (1995) 69–96.
[2] M. Mehrjouei, S. Muller, D. Moller, A review on photocatalytic ozonation used for the treatment of water and wastewater, Chem. Eng. J., 263 (2015) 209–219.
[3] Z.M. He, Y.M. Xia, B. Tang, X.F. Jiang, J.B. Su, Fabrication and photocatalytic property of ZnO/Cu_2O core-shell nanocomposites, Mater. Lett., 184 (2016) 148–151.
[4] Y.C. Ye, H. Yang, H.M. Zhang, J.L. Jiang, A promising $Ag_2CrO_4/LaFeO_3$ heterojunction photocatalyst applied to photo-Fenton degradation of RhB, Environ. Technol., (DOI: 10.1080/09593330.2018.1538261).
[5] Y. Guo, J. Wei, Y. Liu, Y.L. Liu, T.Y. Yang, Z. Xu, Surfactant-tuned phase structure and morphologies of Cu_2ZnSnS_4 hierarchical microstructures and their visible-light photocatalytic activities, Nanoscale Res. Lett., 12 (2017) 181.
[6] Y.M. Xia, Z.M. He, K.J. Hu, B. Tang, J.B. Su, Y. Liu, X.P. Li, Fabrication of n-$SrTiO_3$/p-Cu_2O heterojunction composites with enhanced photocatalytic performance, J. Alloy. Compd., 753 (2018) 356–363.
[7] X.A. Dong, W.D. Zhang, Y.J. Sun, J.Y. Li, W.L. Cen, Z.H. Cui, H.W. Huang, F. Dong, Visible-light-induced charge transfer pathway and photocatalysis mechanism on Bi semimetal@ defective BiOBr hierarchical microspheres, J. Catal., 357 (2018) 41–50.
[8] X.W. Li, W.W. Zhang, W. Cui, Y.J. Sun, G.M. Jiang, Y.X. Zhang, H.W. Huang, F. Dong, Bismuth spheres assembled on graphene oxide: Directional charge transfer enhances plasmonic photocatalysis and in situ DRIFTS studies, Appl. Catal. B-Environ., 221 (2018) 482–489.
[9] C.S. Uyguner-Demirel, N.C. Birben, M. Bekbolet, Elucidation of background organic matter matrix effect on photocatalytic treatment of contaminants using TiO_2: A review, Catal. Today, 284 (2017) 202–214.
[10] S. Challagulla, R. Nagarjuna, S. Roy, R. Ganesan, Scalable free-radical polymerization based sol-gel synthesis of $SrTiO_3$ and its photocatalytic activity, Chemistry Select, 2 (2017) 4836–4842.
[11] Y.X. Yan, H. Yang, X.X. Zhao, H.M. Zhang, J.L. Jiang, A hydrothermal route to the synthesis of $CaTiO_3$ nanocuboids using P25 as the titanium source, J. Electron. Mater., 47 (2018) 3045–3050.
[12] C.K. Chen, S.X. Zhao, Q.L. Lu, K. Luo, X.H. Zhang, C.W. Nan, Topochemical synthesis and photocatalytic activity of 3D hierarchical $BaTiO_3$ microspheres constructed from crystal-axis-oriented nanosheets, Dalton Trans., 46 (2017) 5017–5024.
[13] Z. Chen, H. Jiang, W. Jin, C. Shi, Enhanced photocatalytic performance over $Bi_4Ti_3O_{12}$ nanosheets with controllable size and exposed {001} facets for Rhodamine B degradation, Appl. Catal. B-Environ., 180 (2016) 698–706.
[14] S. Yadav, G. Jaiswar, Review on undoped/doped TiO_2 nanomaterial; synthesis and photocatalytic and antimicrobial activity, J. Chin. Chem. Soc., 64 (2017) 103–116.
[15] Y.B. Liu, G.Q. Zhu, J.Z. Gao, M. Hojamberdiev, R.L. Zhu, X.M. Wei, Q.M. Guo, P. Liu, Enhanced photocatalytic activity of $Bi_4Ti_3O_{12}$ nanosheets by Fe^{3+}-doping and the addition of Au nanoparticles: photodegradation of phenol and bisphenol A, Appl. Catal. B-Environ., 200 (2017) 72–82.
[16] A. Golabiewska, W. Lisowski, M. Jarek, G. Nowaczyk, M. Michalska, S. Jurga, A. Zaleska-Medynska, The effect of metals content on the photocatalytic activity of TiO_2 modified by Pt/Au bimetallic nanoparticles prepared by sol-gel method, Mol. Catal., 442 (2017) 154–163.
[17] D.P. Dutta, A.K. Tyagi, Facile sonochemical synthesis of Ag modified $Bi_4Ti_3O_{12}$ nanoparticles with enhanced photocatalytic activity under visible light, Mater. Res. Bull., 74 (2016) 397–407.
[18] C.X. Zheng, H. Yang, Assembly of Ag_3PO_4 nanoparticles on rose flower-like Bi_2WO_6 hierarchical architectures for achieving high photocatalytic performance, J. Mater. Sci.-Mater. Electron., 29 (2018) 9291–9300.
[19] Y.M. Xia, Z.M. He, J.B. Su, B. Tang, K.J. Hu, Y.L. Lu, S.P. Sun, X.P. Li, Fabrication of magnetically separable $NiFe_2O_4$/BiOI nanocomposites with enhanced photocatalytic performance under visible-light irradiation, RSC Adv., 8 (2018) 4284–4294.
[20] G. Liu, H.G. Yang, J. Pan, Y.Q. Yang, G.Q. Lu, H.M. Cheng, Titanium dioxide crystals with tailored facets, Chem. Rev., 114 (2014) 9559–9612.
[21] F. Wang, H. Yang, H.M. Zhang, J.L. Jiang, Growth process and enhanced photocatalytic performance of $CuBi_2O_4$ hierarchical microcuboids decorated with AuAg alloy nanoparticles, J. Mater. Sci.-Mater. Electron., 29 (2018) 1304–1316.
[22] J. Pan, G. Liu, G.Q. Lu, H.M. Cheng, On the true photoreactivity order of {001}, {010}, and {101} facets of anatase TiO_2 crystals, Angew. Chem. Int. Ed., 50 (2011) 2133–2137.
[23] Y. Bi, S. Ouyang, N. Umezawa, J. Cao, J. Ye, Facet effect of single-crystalline Ag_3PO_4 sub-microcrystals on photocatalytic properties, J. Am. Chem. Soc., 133 (2011) 6490–6492.
[24] J. Jiang, K. Zhao, X. Xiao, L. Zhang, Synthesis and facet-dependent photoreactivity of BiOCl single-crystalline nanosheets, J. Am. Chem. Soc., 134 (2012) 4473–4476.
[25] D. Ariyanti, L. Mills, J. Dong, Y. Yao, W. Gao, $NaBH_4$ modified TiO_2: Defect site enhancement related to its photocatalytic activity, Mate. Chem. Phys., 199 (2017) 571–576.
[26] L.J. Di, H. Yang, T. Xian, X.J. Chen, Enhanced photocatalytic activity of $NaBH_4$ reduced $BiFeO_3$ nanoparticles for rhodamine B decolorization, Materials, 10 (2017) 1118.
[27] H.Q. Tan, Z. Zhao, W.B. Zhu, E.N. Coker, B.S. Li, M. Zheng, W.X. Yu, H.Y. Fan, Z.C. Sun, Oxygen vacancy enhanced photocatalytic activity of pervoskite $SrTiO_3$, ACS Appl. Mater. Inter., 6 (2014) 19184–19190.
[28] Y.H. Lv, W.Q. Yao, R.L. Zong, Y.F. Zhu, Fabrication of wide-range-visible photocatalyst Bi_2WO_{6-x} nanoplates via surface oxygen vacancies, Sci. Rep., 6 (2016) 19347.
[29] A. Tayyebi, T. Soltani, H. Hong, B.K. Lee, Improved photocatalytic and photoelectrochemical performance of monoclinic bismuth vanadate by surface defect states ($Bi_{1-x}VO_4$), J. Colloid Interf. Sci., 514 (2018) 565–575.
[30] Y.C. Huang, B. Long, H.B. Li, M.S. Balogun, Z.B. Rui, Y.X. Tong, H.B. Ji, Enhancing the photocatalytic performance of BiOCl_xI_{1-x} by introducing surface disorders and Bi nanoparticles as cocatalyst, Adv. Mater. Interf., 2 (2015) 1500249.

[31] Y.X. Yan, H. Yang, X.X. Zhao, R.S. Li, X.X. Wang, Enhanced photocatalytic activity of surface disorder-engineered $CaTiO_3$, Mater. Res. Bull., 105 (2018) 286–290.
[32] W. Wei, Y. Dai, B.B. Huang, First-principles characterization of Bi-based photocatalysts: $Bi_{12}TiO_{20}$, $Bi_2Ti_2O_7$, and $Bi_4Ti_3O_{12}$, J. Phys. Chem. C, 113 (2009) 5658–5663.
[33] M. Villegas, A.C. Caballero, T. Jardiel, C. Arago, J. Maudes, I. Caro, Evaluation of piezoelectric properties of $Bi_4Ti_3O_{12}$ based ceramics at high temperature, Ferroelectrics, 393 (2009) 44–53.
[34] D. Urushihara, M. Komabuchi, N. Ishizawa, M. Iwata, K. Fukuda, T. Asaka, Direct observation of the ferroelectric polarization in the layered perovskite $Bi_4Ti_3O_{12}$, J. Appl. Phys., 120 (2016) 142117.
[35] H.C. He, Z.L. He, Z.L. Jiang, J. Wang, T. Liu, N. Wang, A controllable photoresponse and photovoltaic performance in $Bi_4Ti_3O_{12}$ ferroelectric thin films, J. Alloy. Compd., 694 (2017) 998–1003.
[36] K. Qian, Z.F. Jiang, H.Shi, W. Wei, C.Z. Zhu, J.M. Xie, Constructing mesoporous $Bi_4Ti_3O_{12}$ with enhanced visible light photocatalytic activity, Mater. Lett., 183 (2016) 303–306.
[37] H. He, J. Yin, Y. Lia, Y. Zhang, H. Qiu, J. Xu, T. Xu, C. Wang, Size controllable synthesis of single-crystal ferroelectric $Bi_4Ti_3O_{12}$ nanosheet dominated with {001} facets toward enhanced visible-light-driven photocatalytic activities, Appl. Catal. B-Environ., 156–157 (2014) 35–43.
[38] X.X. Zhao, H. Yang, Z.M. Cui, X.X. Wang, Z. Yi, Growth process and CQDs-modified $Bi4Ti_3O_{12}$ square plates with enhanced photocatalytic performance, Micromachines, 10 (2019) 66.
[39] W. Zhao, Z. Jia, E. Lei, L.G. Wang, Z.Y. Li, Y.J. Dai, Photocatalytic degradation efficacy of $Bi_4Ti_3O_{12}$ micro-scale platelets over methylene blue under visible light, J. Phys. Chem. Solids, 74 (2013) 1604–1607.
[40] D.F. Hou, X.L. Hu, P. Hu, W. Zhang, M.F. Zhang, Y.H. Huang, $Bi_4Ti_3O_{12}$ nanofibers–BiOI nanosheets p–n junction: facile synthesis and enhanced visible-light photocatalytic activity, Nanoscale, 5 (2013) 9764–9772.
[41] X. Lin, Q.F. Guan, T.T. Liu, Y. Zhang, C.J. Zou, Controllable synthesis and photocatalytic activity of $Bi_4Ti_3O_{12}$ particles with different morphologies, Acta Phys. Chim. Sin., 29 (2013) 411–417.
[42] Z.W. Chen, X.Y. Jiang, C.B. Zhu, C.K. Shi, Chromium-modified $Bi_4Ti_3O_{12}$ photocatalyst: Application for hydrogen evolution and pollutant degradation, Appl. Catal. B-Environ., 199 (2016) 241–251.
[43] C.X. Zheng, H. Yang, Z.M. Cui, H.M. Zhang, X.X. Wang, A novel $Bi_4Ti_3O_{12}/Ag_3PO_4$ heterojunction photocatalyst with enhanced photocatalytic performance, Nanoscale Res. Lett., 12 (2017) 608.
[44] B. Weng, F. Xu, F. Yu, Fabrication of hierarchical $Bi_4Ti_3O_{12}$ nanosheets on carbon fibers with improved photocatalytic activity, Mater. Lett., 145 (2015) 70–73.
[45] G. Odling, E. Chatzisymeon, N. Robertson, Sequential ionic layer adsorption and reaction (SILAR) deposition of $Bi_4Ti_3O_{12}$ on TiO_2: an enhanced and stable photocatalytic system for water purification, Catal. Sci. Technol., 8 (2018) 829–839.
[46] B. Shi, H. Yin, J. Gong, Q. Nie, Ag/AgCl decorated $Bi_4Ti_3O_{12}$ nanosheet with highly exposed (001) facets for enhanced photocatalytic degradation of Rhodamine B, Carbamazepine and Tetracycline, Appl. Surf. Sci., 419 (2017) 614–623.
[47] Z.M. Cui, H. Yang, X.X. Zhao, Enhanced photocatalytic performance of g-$C_3N_4/Bi_4Ti_3O_{12}$ heterojunction, Mater. Sci. Eng. B, 229 (2018) 160–172.
[48] Y.W. Zhao, H.Q. Fan, K. Fu, L.T. Ma, M.M. Li, J.W. Fang, Intrinsic electric field assisted polymeric graphitic carbon nitride coupled with $Bi_4Ti_3O_{12}/Bi_2Ti_2O_7$ heterostructure nanofibers toward enhanced photocatalytic hydrogen evolution, Int. J. Hydrogen Energ., 41 (2016) 16913–16926.
[49] X.B. Meng, J. Miao, Y. Zhao, S.Z. Wu, X.G. Xu, S.G. Wang, Y. Jiang, Enhanced ferroelectric and UV photocatalytic properties in a $Bi_4Ti_3O_{12}$@ZnO core-shelled nanostructure, J. Mater. Sci.-Mater. Electron., 25 (2014) 1423–1428.
[50] Y. Liu, M.Y. Zhang, L. Li, X.T. Zhang, In situ ion exchange synthesis of the $Bi_4Ti_3O_{12}/Bi_2S_3$ heterostructure with enhanced photocatalytic activity, Catal. Commun., 60 (2015) 23–26.
[51] X.M. Gao, Y. Dai, Y. Zhang, Z.H. Wang, F. Fu, Preparation and photocatalytic performance of spherical-like $Bi_4Ti_3O_{12}$ Composite, Chin. J. Inorg. Chem., 33 (2017) 455–462.
[52] X.X. Zhao, H. Yang, S.H. Li, Z.M. Cui, C.R. Zhang, High photocatalytic activity of large-sized $Bi_4Ti_3O_{12}$ square nanosheets with highly exposed (010) facet, Mater. Res. Bull., 107 (2018) 180–188.
[53] Y.C. Ye, H. Yang, X.X. Wang, W.J. Feng, Photocatalytic, Fenton and photo-Fenton degradation of RhB over Z-scheme g-C_3N_4/$LaFeO_3$ heterojunction photocatalysts, Mater. Sci. Semicond. Proc., 82 (2018) 14–24.
[54] K.S.W. Sing, R.T. Williams, Physisorption hysteresis loops and the characterization of nanoporous materials, Adsorpt. Sci. Technol., 22 (2004) 773–782.
[55] F. Dong, T. Xiong, S. Yan, H.Q. Wang, Y.J. Sun, Y.X. Zhang, H.W. Huang, Z.B. Wu, Facets and defects cooperatively promote visible light plasmonic photocatalysis with Bi nanowires@BiOCl nanosheets, J. Catal., 344 (2016) 401–410.
[56] H. Yang, Q.Q. Liu, F.Y. Li, C.Q. Jin, R.C. Yu, Symmetry of unoccupied electronic states in the high-T_c superconductor $Sr_2CuO_{2+}\delta Cl_{2-y}$ studied by electron energy-loss spectroscopy, Appl. Phys. Lett., 88 (2006) 082502.
[57] H. Wang, W.D. Zhang, X.W. Li, J.Y. Li, W.L. Cen, Q.Y. Li, F. Dong, Highly enhanced visible light photocatalysis and in situ FT-IR studies on Bi metal@defective BiOCl hierarchical microspheres, Appl. Catal. B-Environ., 225 (2018) 218–227.
[58] M.D. Stoller, S.J. Park, Y.W. Zhu, J.H. An, R.S. Ruoff, Graphene-based ultracapacitors, Nano Lett., 8 (2008) 3498–3502.
[59] I.K. Konstantinou, T.A. Albanis, TiO_2-assisted photocatalytic degradation of azo dyes in aqueous solution: kinetic and mechanistic investigations: A review, Appl. Catal. B-Environ., 49 (2004) 1–14.
[60] L.J. Di, H. Yang, T. Xian, X.J. Chen, Construction of Z-scheme g-C_3N_4/CNT/$Bi_2Fe_4O_9$ composites with improved simulated-sunlight photocatalytic activity for the dye degradation, Micromachines, 9 (2018) 613.
[61] L.J. Di, H. Yang, T. Xian, X.J. Chen, Facile synthesis and enhanced visible-light photocatalytic activity of novel p-Ag_3PO_4/n-$BiFeO_3$ heterojunction composites for dye degradation, Nanoscale Res. Lett., 13 (2018) 257.
[62] F. Cardon, W. P. Gomes, On the determination of the flat-band potential of a semiconductor in contact with a metal or an electrolyte from the Mott-Schottky plot, J. Phys. D-Appl. Phys., 11 (1978) L63–L67.
[63] A. Fattah-alhosseini, Passivity of AISI 321 stainless steel in 0.5 M H_2SO_4 solution studied by Mott–Schottky analysis in conjunction with the point defect model, Arab. J. Chem., 9 (2016) S1342–S1348.
[64] X.X. Zhao, H. Yang, R.S. Li, Z.M. Cui, X.Q. Liu, Synthesis of heterojunction photocatalysts composed of Ag_2S quantum dots combined with $Bi4Ti_3O_{12}$ nanosheets for the degradation of dyes, Environ. Sci. Pollut. Res. Int., (https://doi.org/10.1007/s11356-018-4050-3).
[65] S.E. Cummins, L.E. Cross, Electrical and optical properties of ferroelectric $Bi_4Ti_3O_{12}$ single crystals, J. Appl. Phys., 39 (1968) 2268.